Photochemical & Photobiological Sciences

Accepted Manuscript

This is an *Accepted Manuscript*, which has been through the Royal Society of Chemistry peer review process and has been accepted for publication.

Accepted Manuscripts are published online shortly after acceptance, before technical editing, formatting and proof reading. Using this free service, authors can make their results available to the community, in citable form, before we publish the edited article. We will replace this *Accepted Manuscript* with the edited and formatted *Advance Article* as soon as it is available.

You can find more information about *Accepted Manuscripts* in the Information for Authors.

Please note that technical editing may introduce minor changes to the text and/or graphics, which may alter content. The journal's standard Terms & Conditions and the Ethical guidelines still apply. In no event shall the Royal Society of Chemistry be held responsible for any errors or omissions in this *Accepted Manuscript* or any consequences arising from the use of any information it contains.

ROYAL SOCIETY OF CHEMISTRY

www.rsc.org/pps

Photochemical & Photobiological Sciences RSCPublishing

PERSPECTIVE

Tracking the primary photoconversion events in rhodopsins by ultrafast optical spectroscopy

Cite this: DOI: 10.1039/xoxxoooooox

D. Polli,[a] I. Rivalta,[b,c] A. Nenov,[c] O. Weingart,[d] M. Garavelli,[b,c] and G. Cerullo[a]

Received ooth January 2012,
Accepted ooth January 2012

DOI: 10.1039/xoxxoooooox

www.rsc.org/

Opsins are a broad class of photoactive proteins, found in all classes of living beings from bacteria to higher animals, and working either as light-driven ion pumps or as visual pigments. The photoactive function in opsins is triggered by the ultrafast isomerization of the retinal chromophore around a specific carbon double bond, leading to a highly distorted, spectrally red-shifted photoproduct. Understanding, by either experimental or computational methods, the time course of this photoisomerization process is of the utmost importance, both for its biological significance and because opsin proteins are the blueprint for molecular photoswitches. This paper focuses on the ultrafast 11-*cis* to all-*trans* isomerization in visual rhodopsins, and has a twofold goal: (i) review the most recent experimental and computational efforts aimed at exposing the very early phases of photoconversion; (ii) discuss future advanced experiments and calculations that will allow an even deeper understanding of the process. We present high time resolution pump-probe data, enabling to follow the wavepacket motion through the conical intersection connecting excited and ground states, as well as femtosecond stimulated Raman scattering data allowing to track the subsequent structural evolution until the first stable all-*trans* photoproduct is reached. We conclude by introducing computational results for two-dimensional electronic spectroscopy, which has the potential to provide even greater detail on the evolution of the electronic structure of retinal during the photoisomerization process.

Introduction

Retinal or retinylidene proteins, also known as opsins, are a widespread family of photo-sensory proteins, belonging to the wider class of seven-transmembrane domain receptors (7TM), which are found in all domains of living organisms[1]. They are trans-membrane proteins sharing a common tertiary structure consisting of seven α-helices connected to each other by six protein loops[2]. Inside the protein pocket, the chromophore retinal (vitamin-A aldehyde) is attached, through a protonated Schiff base (PSB) linkage, to a Lysine residue in the seventh helix. Opsins can be broadly classified in Type I or bacterial opsins, found in prokaryotes (archeobacteria) and eukaryotes (fungi and algae), and Type II opsins, found in animals possessing image resolving eyes (mollusks, arthropods and vertebrates).

Type I opsins are used by bacteria to harvest light energy using a non-chlorophyll based pathway, in order to carry out metabolic processes. The prototypical one is Bacteriorhodopsin (BR), first discovered in the halophilic archeobacterium *Halobacterium Salinarum*[3]. BR works as a pump for proton transfer across the cell membrane; the ensuing proton gradient is then converted into chemical energy by phosphorylation of ADP to ATP, allowing the bacterium to survive in low-oxygen and high salinity conditions. Another example of light-driven ion pump found in archeobacteria is Halorhodopsin, which acts as a chloride pump[4]. Additional Type I opsins are Sensory Rhodopsins (in archeobacteria) and Channelrhodopsins (in green algae), which behave as light-gated ion channels for the purpose of phototaxis[5]; they serve as the eyes of these primitive organisms, bringing them close to favourable illumination conditions or away from excess light. Halorhodopsins and channelrhodopsins are currently receiving increased attention in optogenetics as actuators for neuronal control[6].

Type II opsins are found in the photoreceptor cells (rods and cones) of the retinas of higher animals[7]. They are a member of the wider class of G protein-coupled receptors (GPCR), which react to an external stimulus by activating a signal transduction pathway and ultimately a cellular response. The opsins found in the rods (Rhodopsin, Rh) are highly-sensitive receptors used for night and peripheral vision, while those found in the cones (Photopsins) are the pigments used for color vision. There are three different types of cone opsins, Photopsin I (found in the L-cones, with absorption peaking in the red), Photopsin II (found in the M-cones and peaking in the green) and Photopsin III (found in the S-cones and peaking in the blue-violet), which are responsible for thrichromic colour vision. Colour tuning is achieved by a combination of electrostatic interaction of the retinal chromophore with charged/polar residues of the protein pocket (electrostatic tuning) and conformational changes in the same chromophore[8]. In all visual opsins, light absorption triggers a series of structural changes in the protein, which activate signal transduction cascades leading to the closure of

the cyclic GMP-gated cation channel and hyperpolarization of the photoreceptor cell, resulting in the conversion of light into an electrical signal[9].

In both Type I and Type II opsins, the primary event is the ultrafast isomerization of the retinal PSB around a specific C=C stretching bond, leading to a highly distorted, spectrally red-shifted photoproduct. In Type I opsins, the PSB starts in the all-*trans* configuration and isomerizes to 13-*cis*[10]; in Type II opsins, the PSB starts from the 11-*cis* configuration (PSB11) and isomerizes to form the primary photoproduct, known as photorhodopsin (photoRh), which in turn relaxes to the first thermodynamically stable all-*trans* retinal photoproduct called bathorhodopsin (bathoRh)[11]. In both cases the photoisomerization reaction takes place on an ultrafast, sub-picosecond timescale (≈200 fs for Rh[12], ≈500 fs for BR[13]) and with very high quantum yield (QY), >60% [14,15]. Remarkably, the speed and efficiency of isomerization in opsins is strongly influenced by the protein pocket. In fact, the retinal chromophore in solution displays much longer excited-state decay times (2–3 ps)[16-18], lower QY (≈20%)[19] and poorly selective photoreactions, with the isomerization taking place around a number of C=C double bonds. In opsins, the photoisomerization process triggers a series of structural changes in the retinal and the surrounding protein, to accommodate for the new shape of the isomerized chromophore, resulting in several reaction intermediates formed on the μs to ms timescales. In both types of opsins the Schiff base is deprotonated during the photocycle, leading to UV absorbing intermediates. However, while the photocycle of Type I opsins is fully reversible, in Type II opsins the Schiff base linkage is cleaved and all-*trans* retinal exits from the protein pocket, requiring metabolic processes outside the protein to regenerate the 11-*cis* retinal1.

Many experimental and computational studies have tried to expose the primary photoconversion events in Type I and Type II opsins. This understanding is of the greatest fundamental and applicative interest because, besides their biological importance, opsin proteins represent the prototypical model for the design of bio-inspired molecular photoswitches, with applications to (opto)electronics[20] and molecular machines[21,22]. Such studies are complicated by the fact that Rh and BR isomerization involves relatively large structural changes in the retinal chromophore occurring over an extremely fast (≈100 fs) timescale, challenging our experimental capability to derive a "molecular movie" of the process. Computational approaches are complicated by the very large size of the protein, preventing a full *ab-initio* treatment of the photoinduced dynamics and requiring approximations that must be formulated judiciously in order to obtain meaningful results.

Photochemical reactions are typically described in terms of a wavepacket moving on a potential energy surface (PES)[23]. Photoexcitation promotes the chromophore from the ground electronic state (S_0) to the first excited state (S_1) of the reactant. Starting from the Franck-Condon (FC) region of the excited state PES, the molecule ends up in the ground state of the photoproduct. There are today a growing number of evidences that these processes in opsin proteins are mediated by conical intersections (CI) connecting the PES of ground and excited electronic states[24,25]. CIs are ubiquitous features in organic photochemistry and photobiology[26,27] and are thought to be responsible for triggering radiationless decays and efficient and ultrafast conversion of photon energy into chemical energy. CIs are molecular geometries in which two (or more) electronic states are isoenergetic, forming a multi-dimensional "seam", which may serve as a doorway for molecules to reach a lower energy electronic state. Depending on the topography around the crossing point, CIs can be classified as "peaked" or "sloped"[28]. In peaked CIs, the molecule is funnelled towards the point of intersection regardless of the direction from which it approaches; in contrast, sloped topographies lead the molecule to the CI less efficiently, resulting in a wider variety of reaction products.

Based on experimental and computational studies, two photophysical models have been proposed for the photoisomerization path of retinal in Type I and Type II opsin proteins: a three-state and a two-state model (Fig. 1(a) and 1(b), respectively). In the three-state model, an avoided crossing between S_1 and a second, higher energy excited state (S_2) occurs along the reaction path, giving rise to a transition state (TS)[29-31] and a small barrier on the S_1 energy profile[32-35] , which the wavepacket needs to overcome before reaching the CI (Fig. 1(a)). In the two-state model, on the other hand, the S_2 state is much higher in energy than the S_1 state and it is not involved in the reaction, which is a barrierless relaxation process from the FC directly leading to the CI (Fig. 1(b))[36,37]. Both these mechanisms assume one-dimensional PES, with a single reaction coordinate, the torsion about the reacting double bond driving the decay along the S_1 energy surface. The general agreement employs the three-state model to describe the isomerization of Type I opsins (such as BR) and the two-state model for Type II opsins (such as Rh). This explains the slower isomerization process of BR (500 fs) with respect to Rh (200 fs): in the first case, the wavepacket has to overcome a barrier before reaching the CI, while in the second case it moves ballistically from the FC point to the photoproduct. Similarly, one could assume that a three-state model is more suitable to describe the photoisomerization of retinal chromophores in solution, given the long excited-state decay time (i.e. few ps) and the low QY (~20%) observed. In proteins, it has been proved by both experiments[38,39] and computations[25,40,41] that the reaction does not only involve the torsion about the reacting double bond driving the isomerization process (C_{11}=C_{12} for Rh and C_{13}=C_{14} for BR), but also other high-frequency normal modes, such as C=C and C-C stretching and hydrogen-out-of-plane (HOOP) motion, especially in the early stages. Therefore the photoisomerization process should be described by wavepacket evolution on a multidimensional PES, going beyond the simplified representation of Fig. 1.

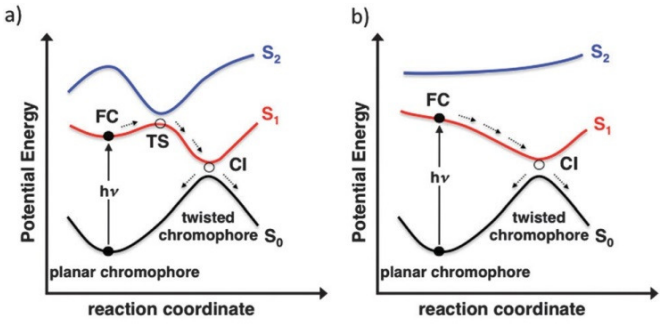

Figure 1 The three-state (panel a) and the two-state (panel b) photoisomerization mechanisms of retinals. In the three-state model, an avoided crossing between the S_1 (in red) and the S_2 (in blue) surfaces gives rise to a transition state (TS) forming a barrier.

This paper focuses on ultrafast spectroscopic studies of the Type II opsin protein Rh, and has a twofold goal: (i) review the most recent experimental and computational efforts aimed at

exposing the very early phases of photoisomerization; (ii) discuss future advanced experiments and calculations that will allow an even deeper understanding of the process. We start by reviewing the different time-resolved experimental techniques: femtosecond pump-probe spectroscopy, femtosecond stimulated Raman scattering and two-dimensional electronic spectroscopy. We then present the current state of the art of computational approaches. We conclude by describing the experimental results comparing them with calculations or, for the case of two-dimensional spectroscopy, by presenting theoretical predictions that may be used to design the most appropriate and informative experiments.

Ultrafast optical spectroscopy

Pump-probe spectroscopy

The principle scheme of a femtosecond pump-probe spectroscopy experiment is reported in Fig. 2(a). A first energetic pulse (the "pump" pulse), resonant with the electronic transition under study, excites the system triggering the excited state dynamics (or a photochemical reaction); the subsequent system evolution is monitored by measuring the transmission change of a weak "probe" pulse as a function of pump-probe delay τ. In broadband (or hyperspectral) pump-probe spectroscopy[42] the probe is a broadband pulse, which is spectrally dispersed on an optical multichannel analyser after the sample. One obtains therefore a differential transmission map, as a function of probe frequency ω_{pr} and pump-probe delay τ (Fig. 2(b)):

$$\frac{\Delta T}{T}(\omega_{pr},\tau) = \frac{T_{on}(\omega_{pr},\tau) - T_{off}(\omega_{pr})}{T_{off}(\omega_{pr})}$$

where T_{on} and T_{off} are the transmission of the probe pulse with and without the pump pulse respectively.

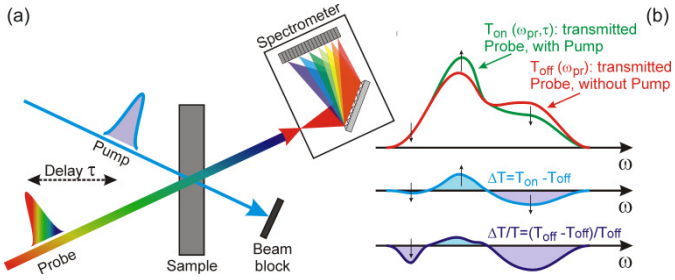

Figure 2: (a) Principle scheme of a femtosecond pump-probe experiment; (b) calculation of the differential transmission signal in broadband pump-probe.

Several signals can be observed in a pump-probe experiment. The pump pulse reduces the number of absorbing molecules in the ground state inducing, at probe frequencies equal or higher than the ground state absorption, an absorption decrease; this is the so-called ground state bleaching (GSB), giving rise to a transmission increase (ΔT/T > 0). At the same time, the pump pulse populates the excited state, so that a probe photon can stimulate it to emit back to the ground state; this stimulated emission (SE) signal, also causing a transmission increase (ΔT/T > 0), occurs at probe frequencies equal or lower than the ground state absorption. For some probe frequencies GSB and SE overlap, while for other frequencies where there is no ground state absorption a pure SE signal can be observed. Finally, the state populated by the pump pulse (either the excited state or the ground state of a photoproduct) can absorb to some other higher-lying level; this so-called photo-induced absorption (PA) causes a transmission decrease (ΔT/T < 0). PA can occur at any probe frequency, depending on the energy level structure of the molecule under study; in particular, it can sometimes spectrally overlap the GSB and SE signals and even overwhelm them.

The time resolution of a pump-probe experiment is determined by the durations of pump and probe pulses[43]. For the pump pulse there is a trade-off between short duration, implying a broad bandwidth, and the need to selectively excite one specific electronic transition. For the probe pulse there is no such limitation and the ideal probe would be a δ-function "white light" pulse[44]. Optical parametric amplifiers (OPAs) are the most widely used sources of energetic tunable ultrashort pulses[45]. An OPA exploits a second-order nonlinear interaction to obtain an optical amplifier with continuously tunable central frequency and, if the process is properly designed, broad gain bandwidth[46]. OPAs in combination with proper spectral phase control (pulse compression) can therefore be used to generate broadly tunable pulses with very short duration, of the order of a few cycles of the carrier wave (i.e. shorter than 10 fs). A system using two independently tunable OPAs[47,48] will be used in the Results and Discussion session to track the photoisomerization dynamics of Rh.

Femtosecond stimulated Raman scattering

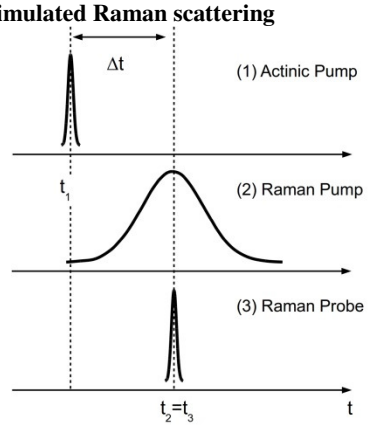

Figure 3. Pulse sequence used in an FSRS experiment.

Pump-probe spectroscopy, while providing a wealth of information on photoinduced processes, intrinsically lacks structural resolution. Time-resolved X-ray[49] and electron[50] diffraction have the capability to observe atomic motions in real time, but they are technically very challenging and have not yet reached the temporal resolution necessary to observe Rh isomerization. Vibrational spectroscopy is a powerful tool to probe structural dynamics, due to the close relationship between vibrational spectra and molecular structures, but until recently it provided only limited temporal resolution. To overcome this limitation, Femtosecond Stimulated Raman Spectroscopy (FSRS) has been introduced as a powerful method for studying chemical and biochemical reaction dynamics and monitoring the structural evolution of a molecule in real time[51-53]. Stimulated Raman Scattering (SRS) is a coherent Raman process involving two synchronized pulses: a narrowband one (linewidth of a few cm^{-1}, corresponding to a pulse duration of a few picoseconds) acting as the Raman pump, and a broadband one, red-shifted with respect to the pump, acting as Stokes pulse. When the pump-Stokes frequency detuning matches a vibrational transition of the system under study, one observes amplification of the Stokes, or stimulated Raman gain. The SRS spectrum delivers the same information on

molecular vibrations as spontaneous Raman, but with much higher signal to noise due to the coherent nature of the interaction process.

In FSRS one acquires SRS spectra of a molecule as a function of the time delay with respect to an ultrashort pulse (the actinic pump, with duration 20-100 fs, see Fig. 3), resonant with an electronic transition of the molecule, triggering a photochemical process. By measuring the changes in SRS spectra induced by the actinic pump, FSRS enables thus to record transient vibrational structures with unprecedented combination of temporal (<50 fs) and spectral (<20 cm^{-1}) resolution, and allows one to follow structural dynamics in photochemical/photobiological processes in real time[54].

Two-dimensional electronic spectroscopy

Two-dimensional electronic spectroscopy (2DES) is an emerging nonlinear spectroscopy technique that transcends the limitations of pump-probe, by achieving simultaneously high spectral and temporal resolution. 2DES provides a wealth of information that usually remains hidden in conventional pump-probe experiments, such as intra- and intermolecular electronic couplings (that are resolved as off-diagonal cross-peaks in a 2D map), pathway-specific signals, homogeneous and inhomogeneous broadening, etc.[55,56]. A 2DES experiment can be schematically described as shown in Fig. 4(a)[57,58]. The system under study is excited by three consecutive pulses, with controllable relative delays t_1 and t_2. This pulse sequence builds up a macroscopic nonlinear polarization in the medium that emits a field, following pulse 3 with a delay t_3. This field is fully measured in amplitude and phase with the help of an additional pulse (pulse 4, known as local oscillator, LO, which can sometimes be the pulse 3 itself). Finally, by Fourier transforming with respect to t_1 and t_3 for a fixed value of the "waiting time" t_2, one derives the 2D spectrum as a function of "excitation frequency" ω_1 and "detection frequency" ω_3. Remarkably, if the excitation pulses are sufficiently short, then 2DES directly measures the third-order nonlinear optical response of the system. Thus 2DES is the "ultimate" time-resolved nonlinear optical experiment, since it provides the maximum amount of information that can be extracted from a system within third-order nonlinear optical spectroscopy. With respect to pump-probe spectroscopy, 2DES has the added experimental difficulty that it requires phase-locking between pulses 1 and 2 (in order to be able to perform the Fourier transform) and between pulses 3 and 4 (for spectral interferometry). This is the reason why 2DES has been experimentally demonstrated only recently and hasn't yet replaced pump-probe spectroscopy, which remains the workhorse for many applications.

2DES can be implemented in two configurations: the heterodyne detected three-pulse photon echo[59,60] and the partially collinear pump-probe geometry[61,62]. Both approaches present advantages but also limitations and technical difficulties. The heterodyne-detected three-pulse photon echo (Fig. 4(a)) exploits the non-collinear interaction geometry between the three driving pulses to emit the four-wave-mixing echo signal in a background-free direction, dictated by phase-matching. The echo signal, proportional to the third-order nonlinear polarization, is fully resolved in amplitude and phase using spectral interferometry with a fourth heterodyning pulse (the LO). The heterodyned signal is detected with a spectrometer, which optically Fourier transforms the signal generating the detection frequency (ω_3) axis; a numerical Fourier transform with respect to t_1 is used to generate the excitation frequency (ω_1) axis. This scheme has the advantage of a background-free configuration but the drawback of requiring interferometric stabilization of two pulse pairs (pulses 1↔2 and 3↔4 respectively). An alternative scheme for 2DES uses a partially collinear pump-probe geometry, with two phase-locked collinear pump pulses and a non-collinear probe pulse, which is dispersed on a spectrometer (Fig. 4(b)). The probe pulse has the dual purpose of generating the nonlinear polarization and heterodyning it (self-heterodyning configuration). Advantages of this configuration are its simplicity and the fact that it automatically measures absorptive 2DES spectra, which are the most direct to interpret. Collinear phase-locked pulses can be generated by a pulse shaper, such as a liquid crystal spatial light modulator[62], an acousto-optic modulator[61], an acousto-optic programmable dispersive filter[63] or alternatively a passive birefringent delay line[64].

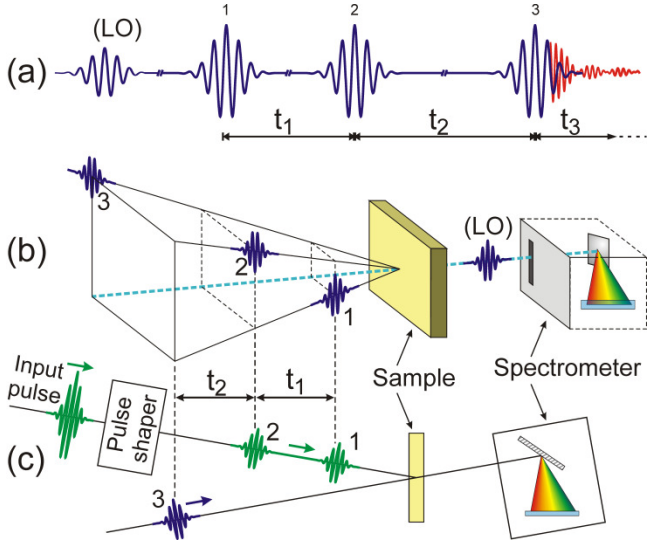

Figure 4. (a) Pulse sequence used in a 2DES experiment. Configurations of the three-pulse photon echo (b) and partially collinear pump-probe (c) geometries.

Numerical modelling

The central mechanistic feature in a photochemical reaction is the intersection space (crossing seam) between the ground and excited state PESs. Any point on this seam (i.e., a CI) provides a funnel for efficient and ultrafast radiationless decay to the ground state. During the last decade computational tools and strategies have been introduced for modelling photoinduced processes[65]. *Ab-initio* quantum mechanical (QM) approaches, such as multiconfigurational complete active space self-consistent field (CASSCF) and multireference perturbative (CASPT2) methods (i.e. the CASPT2//CASSCF approach)[66], have emerged as the elective tools in describing electronic states crossings, their corresponding electronic energy landscape, and the deactivation events involving them. Within a hybrid quantum/classical framework, where surrounding effects are treated by molecular mechanics (MM), a QM/MM approach allows quantitative studies of complex photoactive molecular architectures, such as those of biological photoreceptors. The hybrid QM/MM approach can provide not only atomistic details of the photoisomerization reactions but also fundamental photophysical properties of retinal chromophores that could be used to simulate and predict their transient optical responses. We have recently shown how combination of QM/MM methods with nonlinear response theory (SOS//QM/MM approach) can be used to simulate the third-order nonlinear response of proteic systems with superior accuracy with respect to the most advanced exciton Hamiltonian models[67,68].

Due to the computational cost of *ab-initio* calculations, theoretical studies of photoreactivity have been mainly limited to static topological analysis, i.e. geometry optimization and calculation

of minimum energy paths (MEPs). However, dynamical information such as reaction rates, lifetimes and quantum yields can only be obtained by accurate molecular dynamics (MD) simulations. Photochemical processes start in the FC region of the excited-state PES, where the initial high gradient implies a rapid increase of the kinetic energy. Therefore, the sequence of molecular geometries that represents the course of the photochemical process can deviate significantly from the reaction path obtained by a static analysis. Accurate dynamical information can thus be obtained using QM/MM protocols for direct dynamics, in which potential energies and derivatives are calculated 'on the fly'[69,70]. A swarm of semi-classical QM/MM trajectories can be computed including the possibility of hopping between PESs, thus modelling the excited state dynamics and decay through the seam. This approach avoids the choice of an *a priori* reaction coordinate and, with a sufficiently high number of trajectories, delivers a statistically meaningful picture of the process. This statistical information can also be used to accurately characterize the nonlinear optical response of the system, allowing for inclusion of signal broadenings. The methodology is discussed in detail in the following subsection.

QM/MM Surface Hopping Dynamics

Combined QM/MM methods divide large atomistic systems, e.g. proteins, into two or more layers that are treated with different computational accuracy. The active site of a protein or the photoactive component of a receptor is usually treated at the highest QM level, while the remaining protein backbone, solvent and/or membranes are calculated with a force field method. Care must be taken of the connection sites between these two regions. A common method is to use a link-atom scheme, where the dangling bonds of the QM subsystem are saturated with hydrogen or other atoms/groups. Link atom force components are redistributed among its direct QM and MM neighbours to restrict their motion along the QM-MM connection axis[71].

The subtractive QM-MM scheme adds the energies of the whole system computed at the MM level (S) and the energy of the QM-layer (I) plus link atoms (L); double counting of energies is 'corrected' by subtracting the MM-energy of the high layer with link atoms:

$$E_{QM/MM}(S) = E_{MM}(S) + E_{QM}(I+L) - E_{MM}(I+L)$$

i.e. this method requires a full MM setup and parameters for the system under study. For a precise modelling of the interaction between QM and MM subsystems, and especially for the computation of accurate absorption energies, the wave function *must* be polarized at least by the surrounding point charges of the MM atoms. Resulting force contributions onto the MM gradients can be obtained by computing the electric field from the QM wavefunction. Ideally, the inclusion of polarizabilities via polarizable force fields[72] will further enhance the description. Until now, however, no general scheme provides stable gradients for QM/MM dynamics computations. To reduce the artefacts due to overpolarization at the QM/MM boundary, a charge repartitioning scheme is employed: it deletes the charge of the border atoms on the MM side, redistributing it among its MM neighbours[69].

Initial conditions for dynamics simulations can be generated via a zero-point energy sampling scheme. After geometry optimization and harmonic frequency computation, potential energies and velocities for each mode are chosen randomly with the constraint that kinetic and potential energy represent the zero-point energy ½ħω of the specific mode[73]. Summing up all velocity and coordinate displacements for each mode generates a starting configuration and initial velocities for an individual dynamics trajectory computation. In order to obtain statistically relevant results, this procedure is repeated to generate an ensemble of starting conditions, representing a wave packet that oscillates around its ground-state minimum with zero-point energy (see Fig. 5). Temperature effects can be included by considering higher vibrational excitations of the normal modes, according to a Boltzmann distribution.

High-frequency oscillations often generate problems in classical Newtonian dynamics. Temperature levels high above the 'classical' temperature are easily reached when the suggested sampling scheme is pursued. This requires the use of very short time steps in the dynamics propagation in order to correctly sample the resulting fast atomic motions. Often, such vibrations play only a minor role for the ultrafast photochemistry of the system under study. Thus, high frequency C-H, N-H or O-H vibrations may be excluded from the sampling without major loss of accuracy.

For the simulation of the photoinduced dynamics, the computed ground-state ensemble is vertically excited to a corresponding excited singlet state. The probability for the excitation of an individual trajectory in the ensemble can be computed by considering and normalising the corresponding oscillator strengths among the ensemble, deciding whether the trajectory will be a member of the excited state wavepacket and in which excited state the trajectory starts.

To follow the dynamics it is necessary to compute all involved potentials (ground and excited states) simultaneously. The CASSCF-state-average (SA) approach delivers energies for all states of interest with reasonable accuracy. Preferably, only those states are included in the averaging among which transitions can occur. The averaging procedure furthermore requires corrections to the gradient, which are available through computation of the coupled-perturbed multi-configurational self-consistent field equations[74] or by evaluating multi-configurational linear response terms[75].

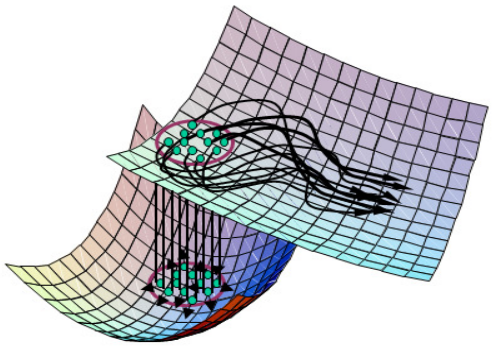

Figure 5. Individual trajectories oscillating in ground state harmonic potential get vertically excited and move in the S_1 state starting from the FC region.

The excited state trajectory is computed by propagating the nuclear motions with a velocity Verlet algorithm[76]. When the energy between two states reaches a certain limit (40 kcal/mol in our case), the MD step size is reduced and non-adiabatic coupling matrix elements are computed. The probabilities for remaining in the current state or hopping to another state are evaluated and compared to a random number, following Tully's fewest switches algorithm[77]. The time-dependent electronic wavefunction between the last and the actual MD step is therefore propagated (using a step ca. 100-200 times smaller than the actual MD step) under the assumption that inter-state coupling terms change linearly during this interval[78]. It must be noted that this approach yields an ensemble description that overestimates the coherence between ground- and excited-state wavepacket motions. This can be partly accounted for by applying the empirical decoherence-correction scheme suggested by Granucci *et al.*[79]. If a hop is induced and an energy gap exists between the two

involved states, the velocity is scaled along the derivative coupling vector. To minimize any interference with product generation, we compute the direction of maximum overlap between the velocity vector and the derivative coupling vector and only scale along the estimated direction. Once the hop to the other surface is performed, the gradient of this surface is used to propagate the nuclear motions.

In many cases the continuous usage of the CASSCF state-average scheme after the surface hopping to the ground state leads to problems (such as convergence errors and root flipping) which will affect the potential and the forces in the corresponding trajectory. In these cases, a switch to single-state CASSCF is invoked when the energy difference between the excited and the ground state is sufficiently large (40 kcal/mol). Comparative computations showed that an abrupt switch (directly from SA with weights 0.5/0.5 to single state) has a lower influence on gradients and velocities than a smooth switch along several MD steps.

For the simulations shown in this paper, a full CASSCF(12,12)//Amber treatment with the 6-31G* basis set was applied for reaction path optimizations.. The Molpro suite of programs was used for QM computations, and the Amber FF99 force field for the MM part. A reduced CAS(10,10) active space was generated for ground state optimization, frequency computation and excited-state dynamics. S_1 state dynamics were computed by averaging equally over the lowest three (Rh) or lowest two CASSCF states (isoRh). Further details are given in the corresponding sections.

Results and discussion

Pump-probe spectroscopy

Femtosecond pump-probe experiments were performed on bovine Rh molecules extracted from the rod outer segments of bovine retinae and purified by sucrose flotation followed by sucrose density gradient centrifugation[80]. The photochemical reaction was initiated by excitation of the retinal chromophore with 10-fs pulses centred at 520 nm, resonant with the ground-state absorption. The photo-induced dynamics were then probed by delayed pulses either in the visible range (from 500 to 720 nm, with ~7 fs duration) or in the near-Infrared (NIR, from 820 to 1020 nm, with ~13 fs duration), both generated by broadband OPAs. Figure 6(c) shows a two-dimensional ΔT/T map as a function of probe wavelength and delay[81]. Immediately following excitation, we observed a positive signal (blue in the figure) with maximum intensity at ~650 nm, which can be assigned to SE from the excited state, due to the negligible ground-state absorption in this wavelength range. The SE signal rapidly shifts to the red while losing intensity and disappearing to wavelengths longer than 1000 nm within ~75 fs. At this time, the ΔT/T signal changes sign and turns into a weak PA signal (yellow in the figure), which first appears at 1000 nm and then gradually blue shifts and increases in intensity. For delays longer than 200 fs, the PA signal stabilizes to a long-lived band peaking at 560 nm, indicating the presence of the all-*trans* photoproduct. We emphasize that the use of a sub-20 fs NIR probe is the key to observing the reacting molecule with a remarkably small temporal gap between the excited and ground electronic states. Time traces at selected probe wavelengths are shown in Fig. 6(a), highlighting the red shift of the SE signal and the subsequent blue shift of the PA.

To extract a dynamic model of the photoinduced process from these data we simulated the transient signals ($S_1 \rightarrow S_0$ SE, $S_1 \rightarrow S_2$ PA and $S_0 \rightarrow S_1$ PA) by averaging over a room-temperature sample of QM/MM trajectories tracking the Rh-embedded chromophore excited state/ground state evolution, including excited-state decay as described in the section Numerical Modelling. Virtual spectroscopies and dynamics (Figs. 6(b) and 6(d)) agree almost quantitatively with the experimental results. The same holds for the 61% photo-isomerization quantum yield and ~110 fs average $S_1 \rightarrow S_0$ hopping time extracted from the simulations, thus further supporting the reliability of the theoretical approach[81].

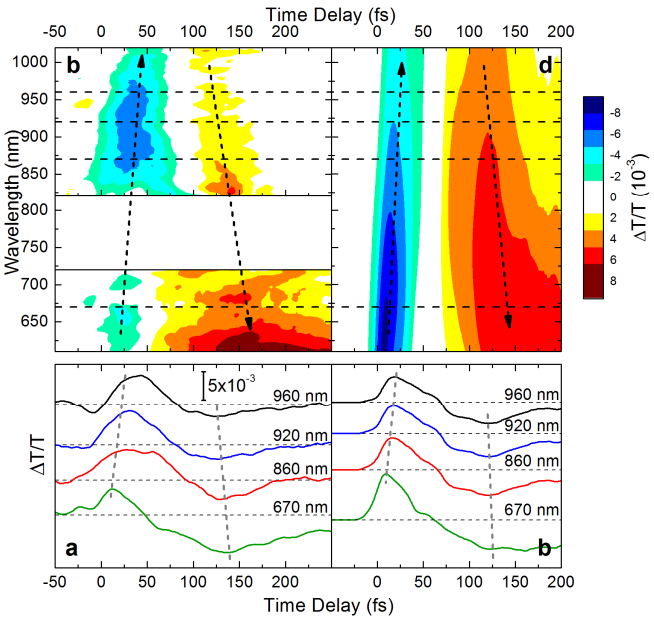

Figure 6. Wavepacket dynamics through the Rh conical intersection. Experimental (a) and simulated (b) time traces at selected probe wavelengths (as indicated). Experimental (c) and simulated (d) ΔT/T map as a function of probe delay and wavelength in the visible and NIR spectral regions. Gray lines are a guide to the eye highlighting the shifts of the SE and PA signals in time. Adapted from Ref. [81].

The ultrafast complex spectral evolution observed both experimentally and theoretically can be understood qualitatively with the help of the simplified one-dimensional model shown in Fig. 7. Here, the motion of the wavepacket is depicted along the ground and excited state PESs of the Rh chromophore as a function of the isomerization coordinate. The wavepacket initially created in the FC region of the excited state of the 11-*cis* reactant rapidly evolves along the reaction pathway towards the CI, and the SE progressively shifts to the red as the band gap between the excited and ground states narrows. Near the CI region, which is reached in ~80 fs according to both experiments and simulations, the SE signal vanishes as the two surfaces approach each other and the transition dipole moment decreases. Following the "jump" to the hot ground state of the photoproduct, a symmetric PA signal is formed. This PA band rapidly shifts to the blue as the surfaces move away from each other energetically and the wavepacket relaxes to the bottom of the photoproduct well, reflecting the redistribution of the excess energy deposited in the molecule and the final torsional movement to the all-*trans* configuration.

To complete the description of photo-induced dynamics in Rh, we report the portion of the ΔT/T map probing the response of the system in the visible region, from 495 nm to 610 nm (Fig. 8(a)). In agreement with previous studies[12,82,83], we observe the delayed formation of the PA band of the photoRh photoproduct, which peaks at 560 nm and is complete within

200 fs. The signal does not display exponential build-up dynamics, but rises rather abruptly starting at ~150 fs (see Fig. 8(b)), which is the time needed for the wavepacket to cross the CI and enter the probed wavelength window on the photoproduct side. The blue region of the spectrum is dominated by the GSB signal from the ground state of the parent Rh molecule, peaking at ~510 nm. These two spectral signatures partially overlap so that the GSB band shrinks in time as the photoproduct PA signal forms and blue shifts. The GSB amplitude also decreases due to the return of the 35% unsuccessful excitations back to the ground state of the reactant. At early probe delays, a PA band peaking at ~500 nm is evident, due to a transition from the FC excited state to a higher-lying S_n state[11,82], having a greater dipole moment than the ground state GSB. This band disappears within ~50 fs, as the wavepacket moves out of the FC region.

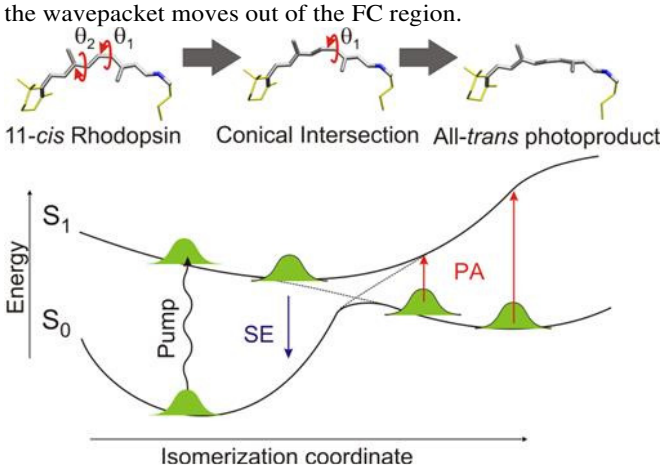

Figure 7 Sketch of the ground- and excited-state PES of the retinal chromophore in Rh as a function of the isomerization coordinate. It shows that SE from the excited state of the parent molecule and PA from the hot photoproduct can monitor the wavepacket dynamics through the CI. On top averaged structures of the chromophore at the initial 11-*cis*, CI and final all-*trans* configurations; gray/yellow colours indicate the chromophore QM/MM mobile regions in the simulations.

The extremely high experimental time resolution combined with the remarkable agreement with theory makes it possible to confidently predict the real-time structural changes occurring within the first 200 fs of retinal isomerization in Rh. Fig. 7 shows in its upper panel the key structures, namely the 11-*cis* reactant, the structure of retinal at the CI and the photoRh photoproduct. Comparison of the retinal structure in the ground state with the structure at the CI reveals dramatic changes only in the vicinity of the isomerizing bond. We found that the average C_{11}=C_{12} dihedral angle at the CI is θ_1~-87.8°, ranging from -75° to -105° for individual trajectories, emphasizing the relevance of the C_{11}=C_{12} twist in triggering internal conversion (Fig. 9(a)). At the same time, the C_9=C_{10} torsional angle θ_2 also exhibits a large change (by ~45°) on the excited-state surface as the wavepacket moves towards the CI (Fig. 9(b)). This torsion also persists on the photoproduct side, accounting for chromophore ends that are motionless during the isomerization process, in agreement with structures derived from FSRS[84] and reminiscent of Warshel's bicycle pedal proposal [85, 86]

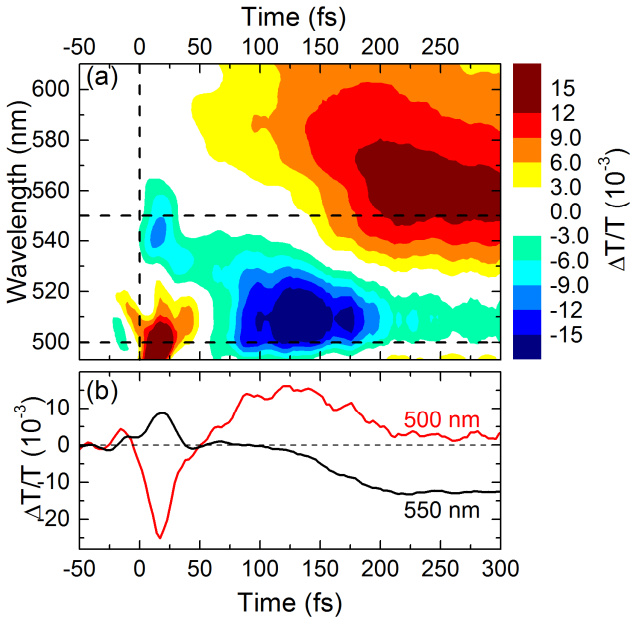

Figure 8 Rh isomerization probed in the visible spectral range. (a) ΔT/T map in the visible spectral region. (b) Time traces at 500 nm and 550 nm probe wavelengths. Adapted from Ref. [81].

The combination of high time resolution experimental data and high accuracy numerical simulations has allowed us to expose the complete molecular dynamics of Rh photoisomerization and thereby understand how it achieves its unique reaction speed. The structural evolution from the reactant towards the CI is restricted almost exclusively to the atoms in the centre of the molecule. This behaviour is promoted by the tight binding pocket provided by the protein to the chromophore, which restricts the possible motion at its ends through non-covalent interactions[87]. Therefore, retinal can use all of the incident photon energy to drive minimal atomic displacements in the relevant region and reach the CI region within 80 fs, resulting in a very fast reaction speed. Once the local isomerization has taken place, the overall highly strained structure can then relax in the photoproduct well to result in the more *trans*-like structure, which completes the primary isomerization reaction in Rh (see the following paragraph on the FSRS results). These observations are consistent with a CI having a strongly peaked topography, leading to a very efficient ballistic transfer of the molecular wavepacket from the 11-*cis* reactant to the all-*trans* photoproduct and to the very high quantum efficiency of the visual response.

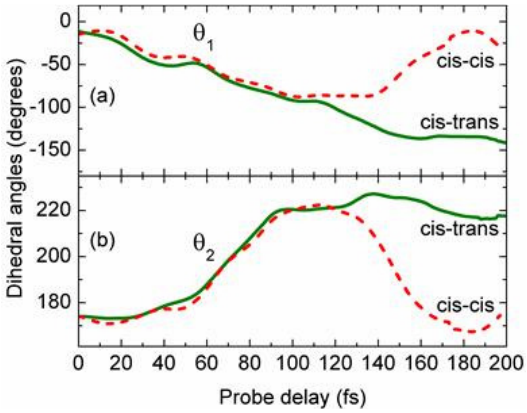

Figure 9 Torsional angles θ_1 and θ_2 during isomerizing trajectories (solid line) and in non-isomerizing paths (dashed lines). Adapted from Ref. [81].

Pump-probe spectroscopy of Isorhodopsin

We have already discussed how the photoinduced activity of the retinal PSB11 is radically different in the protein with respect to a solution environment. However, also the specific configuration of the chromophore within the protein pocket plays a key role in enhancing the reactivity of the visual pigment. To improve our understanding of the link between molecular structure and isomerization efficiency in the visual rhodopsins, we have studied the visual pigment analog Isorhodopsin (isoRh), which embeds 9-*cis* retinal (PSB9) instead of 11-*cis*, while sharing the same opsin environment. IsoRh can be generated by illuminating Rh with laser radiation at 568 nm for 30 min at 77 K. Its photoisomerization is slower (it is completed in ≈600 fs[88]) and less efficient (QY≈0.2[89]) than Rh, but it results in the production of the same bathoRh intermediate[90], so that Rh, bathoRh and isoRh form, upon irradiation, a steady-state three-component photoequilibrium[91]. Using the same high time resolution broadband pump-probe set-up as for Rh, we followed the ultrafast isomerization of isoRh in the visible and in the near-infrared[92].

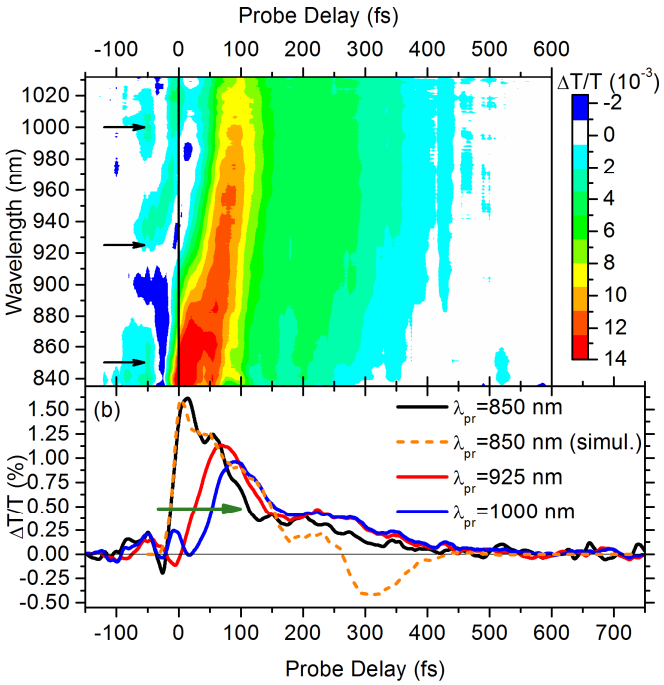

Figure 10. (a) ΔT/T map of isoRh in the NIR range, following excitation by a 10-fs pulse at 500 nm; (b) solid lines: time traces at selected probe wavelengths; dashed line: MD-simulated trace at 850 nm. The green arrow highlights the delayed formation of the SE for longer wavelengths. Adapted from Ref. [92].

In the visible it is particularly difficult to disentangle the different transient PA signals (from the excited state of the reactant, from the hot ground state of the non-isomerized reactant and from the isomerized all-trans photoproduct). In the NIR spectral region (Fig. 10(a)), on the other hand, such spectral congestion is relieved, and we directly probe the excited state of the reactant via its SE. We observe an instantaneous rise of the signal at short wavelengths, which rapidly shifts to longer wavelengths because the energy gap between ground and excited states decreases as the wavepacket moves towards the CI, similarly to Rh. The SE signal shows a strongly non-exponential decay, with an early fast component completed within approximately 150 fs, followed by a weaker plateau that persists until ~400 fs delay (see Fig. 10(b)). This two-component decay of the SE is radically different from what observed in Rh and it is not consistent with the picture of a single wavepacket that ballistically moves through a CI.

To unravel the mechanistic rationale underlying such spectral signatures, we employed a similar approach to Rh, calculating the evolution of the opsin-embedded PSB9 chromophore from the excited to the ground electronic state over a statistically meaningful set of hybrid QM/MM trajectories[92]. For the dynamics we employed *ab initio* (CASSCF(10/10)/6-31G*//Amberff99) with electrostatic embedding and initial conditions and dynamics computations as stated in the section Numerical Modelling. The MD time step was 0.5 fs, reducing to 0.25 fs near the CI region. The results obtained, in agreement with recent calculations on isoRh[93] performed at lower computational level (CAS(6,6)/6-31G), show a wavepacket dynamics which is strikingly different from that observed for Rh. As schematically reported in Fig. 11, the wavepacket initially created in the PSB9 FC region branches within ~30 fs and almost equally populates two competitive radiationless decay routes. The first proceeds without major hindrance along counter-clockwise motion of the H-C_{10}-C_{11}-H fragment, involving a "reverse" pedal motion (i.e. a positive twist along C_9=C_{10} and strong negative twist along C_{11}=C_{12}) similar to Rh isomerization into photoRh. This path leads within ~160 fs to a CI (named here CI_1(++)) which is unproductive: molecules either revert back to the ground state of the reactant or undergo a strong twist along the C_{11}=C_{12} dihedral thus forming a di-cis photoproduct. The second decay route is delayed (mainly due to interactions between H-C_{11} and TYR268 residue in the forward path), featuring an extended energy plateau and forward pedal rotation (i.e. strong negative C_9=C_{10} rotation and positive torsion at C_{11}=C_{12}). It leads within ~280 fs to a CI (called here CI_2(--)) which can generate the all-*trans* photoproduct with a quantum yield of 16±4%, in good agreement with experimental observation (22%). The two decay channels are responsible for the experimentally observed non-exponential two-component decay of the SE signal (see dashed line in Fig. 10(b)) and for the slower 600-fs all-*trans* photoproduct formation observed in isoRh compared to Rh.

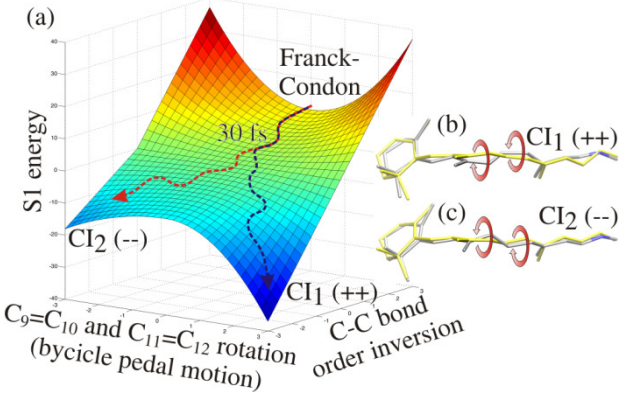

Figure 11. (a) Model of isoRh S_1 potential energy surface along bicycle pedal motion and bond inversion coordinates. (b)-(c) Averaged structures of the chromophore at the CI_1 and CI_2 configurations respectively (grey) compared with the FC configuration (yellow). The red arrows indicate the reverse/forward bicycle pedal motions. Adapted from Ref. [92].

These results clearly show that, despite sharing the same apoprotein environment, Rh and isoRh display a remarkably different photochemistry, caused by the different configuration of the retinal

chromophore and its steric interactions. The photoreactions in both proteins are, nevertheless, triggered by a unique reaction coordinate, that is bicycle pedal motion along the C9=C10 and C11=C12 double bonds. In the protein pocket 9-*cis* retinal operates in both forward and reverse bicycle pedal directions, while the forward path is blocked for 11-*cis* retinal. In both compounds, the fast decay channel is associated with reverse bicycle pedal motion. In isoRh this deactivation path is non-productive; reaction toward photoRh proceeds only in the forward direction, featuring extended steric interactions with the protein environment and thus significantly slower reaction time. Thus Rh and isoRh share a common valley on the excited state PES, just starting from opposite ends[94]. The branching of the excited state population into slower productive and faster unproductive channels explains the reduced activity and quantum yield in isoRh as compared to Rh, where only the fast and productive path is populated and a higher QY obtained. Thus the photoisomerisation in isoRh proceeds via a two-channel decay mechanism, while the direction of torsion in Rh is unique.

Femtosecond stimulated Raman scattering

By tracking time-dependent molecular structures, FSRS provides new insights, complementary with respect to those of pump-probe, on the mechanism of Rh isomerization and on the reasons for its speed and efficiency. Kukura *et al.* performed FSRS experiments on Rh following excitation by a 30-fs actinic pump a 500 nm[84]. A narrowband Raman pump at 800 nm and a broadband near-IR Stokes pulse were used to acquire the transient SRS spectra. Due to the speed of the isomerization process in Rh and to the limited temporal resolution available, FSRS follows the structural evolution of Rh on the ground state of the photoproduct, after the CI, starting at ≈200 fs delay. It is thus an ideal complement to the pump-probe results presented in the previous paragraphs. Figure 12 shows a sequence of FSRS spectra for Rh in the 800-1600 cm^{-1} region, which contains the most structurally relevant modes: the ethylenic C=C stretch at ≈1550 cm^{-1}, the C–C single-bond stretching and C–H rocking modes in the so-called fingerprint region (1100 to 1300 cm^{-1}), and the HOOP modes between 800 and 1000 cm^{-1}. For comparison, the figure also reports spontaneous Raman spectra of the Rh reactant and the bathoRh photoproduct: they show small but significant changes in frequency and intensity in both the ethylenic and fingerprint modes. Larger changes are observed in the HOOP region, in which the spectrum evolves from a single peak in Rh at 970 cm^{-1}, due to the $C_{11}H{=}C_{12}H$ HOOP motion, to three bands at 920, 875, and 850 cm^{-1} in bathoRh, assigned to the isolated C_{11}–H, C_{10}–H, and C_{12}–H hydrogen wagging modes, respectively. The FSRS spectra reveal a narrowing and a blue-shift of the C=C peak on the picosecond timescale, which is consistent with vibrational energy dissipation on the ground state of the photoproduct PES. In the fingerprint region, the FSRS spectrum of photoRh at 200-fs delay appears to be midway between that of the Rh reactant and that of the relaxed bathoRh photoproduct and evolves on the picosecond timescale, with the peak at 1267 cm^{-1} losing intensity, while those at 1216 and 1237 cm^{-1} remain essentially unchanged. The most dramatic evolution, however, is observed in the HOOP region, with dispersive, derivative-like lineshapes which evolve within 1 ps to the three peaks characteristic of bathoRh. This dispersive lineshape is typically observed in FSRS when detecting a mode whose frequency changes over a timescale comparable to that of vibrational dephasing[53,95]. Such lineshapes can be simulated rather accurately (red lines in Fig. 12(a)) by assuming that the HOOP frequencies increase by 100 cm^{-1} from 200 fs to 2 ps, with a 325-fs time constant (see Fig. 12(b)). This blue-shift of the HOOP frequencies with time can be understood by recalling that the frequency of the wagging modes is very sensitive to the restoring force of the retinal backbone[96]. An out-of-plane distortion of the backbone thus results in a decrease of the conjugation length and a lowering of the wagging frequency. Thus the HOOP frequencies are minimum in the highly distorted photoRh and then progressively increase as the molecule evolves to the more planar bathoRh state.

The FSRS data clearly show that a significant part of the structural evolution leading to the equilibrium all-*trans* photoproduct takes place on the ground state PES along slow torsional coordinates, whereas the excited state decay is promoted by fast HOOP coordinates. The overall structure of retinal in photoRh is more similar to that of the reactant than of the final product bathoRh, which is not surprising given the extremely rapid formation of this state, but clearly calls for a multi-dimensional isomerization model, driven by more than one vibrational coordinate[40,41]. FSRS data also enable to understand the role of the tight protein binding pocket in promoting the reaction and maximizing its QY: (i) by pretwisting the retinal backbone, it primes the molecule for rapid excited-state decay along the HOOP coordinate; (ii) it restricts the possible motion of the excited chromophore through steric interactions with surrounding amino acids; and (iii) it captures the high-energy bathoRh product and efficiently transfers this energy into protein conformational changes that activate signal transduction cascades.

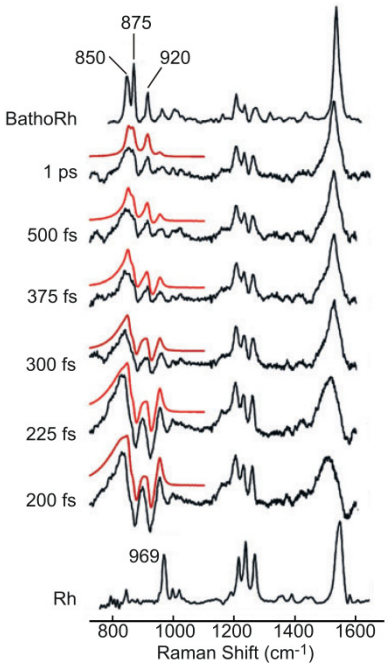

Figure 12: Selected time-resolved FSRS spectra of Rh following excitation by a 30-fs pulse. Conventional resonance Raman spectra of the Rh reactant and the bathoRh photoproduct are included for comparison. Theoretical simulations of the HOOP features are indicated in red. Adapted from Ref. [84].

Two-dimensional electronic spectroscopy

So far, 2DES data of Rh isomerization have not been reported. Here we present results of state-of-the-art numerical simulations that show the power of the technique and should help in designing the most effective 2DES experiments[97].

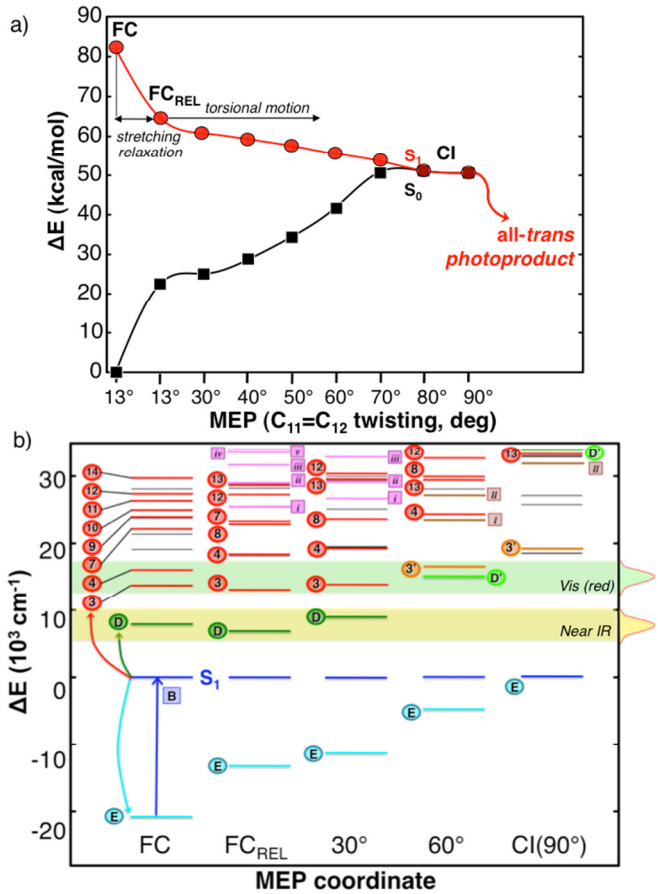

Figure 13 (a) MEP of PSB11 photoisomerization calculated at the CASPT2//CASSCF level from the FC point to the twisted CI funnel. (b) Evolution of the excited states manifold along the MEP. For selected critical points ground state (GS) (cyan lines), S_2 state (green lines), high-lying excited states (bright states in red or orange and dark states in black) energies are reported, with zero-energy set at the S1 state (blue lines). Stimulated emission (E), GS bleaching (B), $S_1 \rightarrow S_2$ (D and D') transitions and excite state absorptions to higher-lying states are also depicted as arrows in the FC region (for simplicity). Magenta and brown lines are used to indicate states absent in the FC point. Green and yellow bars indicate the NIR and Vis (red) spectral regions, respectively, of PAs. Reproduced from Ref. [97].

Figure 13 shows the MEP of the retinal photoisomerization pathway in bovine Rh (from the FC region to the CI funnel) calculated at the CASPT2//CASSCF level within a hybrid QM/MM scheme (Fig. 13(a)) and the evolution of the excited states manifolds on some selected MEP points (Fig. 13(b), where the zero-energy is set at the S1 state on each MEP point). The excited state branch of the photoisomerization pathway is characterized by initial skeletal deformations (i.e. a bond order inversion, FC_{REL}) followed by a torsional motion of the C_{11}=C_{12} central bond from ~13° to ~90°, where the CI is found, according to the previously mentioned two-state two-mode model[25]. Upon photoexcitation to the spectroscopic S_1 state, corresponding to the single Homo-Lumo (H→L) excitation, the initial bond inversion induces some significant changes in the electronic structure of the chromophore. In particular, a reduced S_0/S_1 energy gap and consequent large red-shift of the $S_1 \rightarrow S_0$ SE (transition E) is observed, along with a blue-shift of some ionic excited states (transitions 4 and 7) and stabilization of some high-lying excited states that were not present in the FC region (i.e. transitions i-v). Interestingly, the transitions involving the covalent S_2 and S_3 states, corresponding to the double H⇒L (transition D) and H,H-1⇒L (transition 3) excitations, respectively, are not significantly affected by the skeletal relaxation and the corresponding PA signals are expected to appear in the NIR (see yellow bar in Fig. 13(b)) and in the visible (see green bar in Fig. 13(b)) regions, respectively. The initial twisting along the central bond does not involve major changes of the excited states manifold and remarkable alterations are observed only for twisting angles larger than 30°. In particular, a localization of the CASSCF active orbitals is found at 60°, changing the overall electronic structure of the chromophore and inducing large blue-shifts of the PA bands and red-shift of the SE band. The PA signals that survive upon rotations of 60° are those involving the covalent S_2 (now transition D') and S_3 states (now transition 3') that fall in the red region of the visible spectrum (at ~15000 cm^{-1}). These PAs are further blue-shifted while remaining bright (i.e. with oscillator strength larger than 0.02) at the CI, where the torsional rotation reaches 90°.

In the previous sections we have shown how QM/MM simulations can be used to reproduce quantitatively the pump-probe spectroscopic data of PSB11 isomerization in Rh (Fig. 6(b)), and that the calculated MEP indicates a barrierless process following a two-state photoisomerization mechanism (Figure 1(b)). This outcome indicates that in the protein environment the S_1/S_2 energy gap is large and there is no coupling between the energy surfaces of the ionic S_1 and the covalent S_2 states during the photoisomerization. Instead, such interplay is expected to have an important role in the photochemistry of retinal chromophores in solution, following a three-state photoisomerization mechanism[98]. Ultrafast optical spectroscopy, in its pump-probe or 2DES schemes, could in principle be used to decipher the mechanistic differences of retinal photochemistry in various environments by probing the relative positions of the S_1 and S_2 states during the ultrafast photoisomerization. However, 2DES offers the unique capability to resolve inhomogeneous broadening of the different signals along the pump frequency axis, which cannot be measured using conventional pump-probe spectroscopy. Since 2DES allows monitoring the photoisomerization process with the best possible combination of spectral and temporal resolution, here we focus on simulations of 2D spectra using different combinations of pulse frequencies in order to follow the evolution of specific signals (i.e. the $S_1 \rightarrow S_2$ transitions) during the PSB11 photoisomerization. The 2DES *degenerate* (one-colour) setup would be the simplest combination of pulses, involving identical pump and probe pulses with central frequencies at the PSB11 absorption maximum, ν_{MAX}. However, the major contributions to the time-resolved one-colour 2D spectra will be the negative GSB and SE signals overlapping with positive PA bands coming from high-lying excited states[97]. Thus, in order to track the energy gaps between the ionic spectroscopic state and low-lying covalent excited states (i.e. S_2 and S_3), a *two-colour* setup with probe pulse frequencies lower than ν_{MAX} is required. The evolution of the excited states manifold depicted in Fig. 13(b) suggests that probe pulses in the NIR and in the red visible regions should be employed to follow the evolution of the $S_1 \rightarrow S_2$ transition (D and D' signals) along the PSB11 photoisomerization pathway.

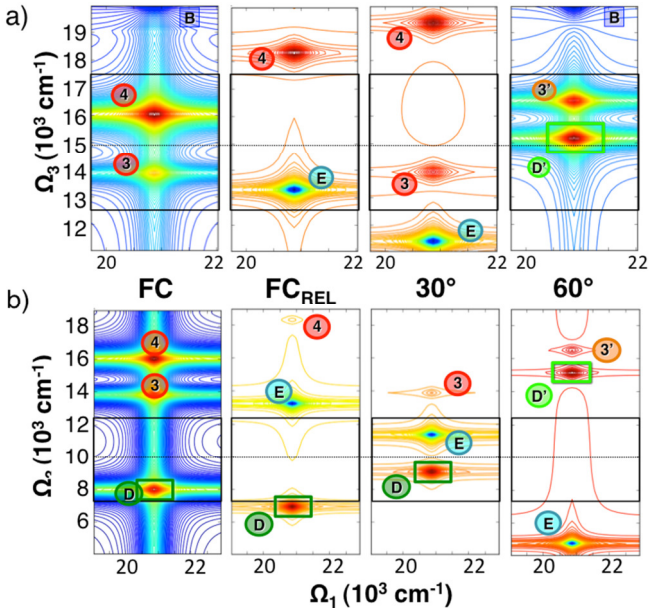

Figure 14. Simulated 2D (xxxx) spectra for the *two-colours* 2DVis (panel a) and the two-colour 2DVis/NIR (a) setups. 2D spectra are reported for the selected MEP point from the FC to the 60° structure. The complex part of the signal is plotted on a logarithmic scale. The peaks are labelled according to transitions assignment of Figure 13. Black boxes indicate the used 5000 cm^{-1} bandwidth and central frequencies are indicated with dotted lines. Reproduced from ref [97].

Figure 14 shows the 2D spectra simulated at selected MEP points (i.e. FC, FC$_{REL}$, 30° and 60°) using two different two-colours setups: the first with pump pulses centred at ν_{MAX} (Ω_1=20875 cm^{-1}) and probe pulse centred at Ω_3=15000 cm^{-1} (2DVis(blue/red), see Fig. 14(a)) and the second with probe pulse centred at Ω_3=10000 cm^{-1} in the NIR (2DVis/NIR, see Fig. 14(b)). The latter setup is particularly suited to obtain spectroscopic signatures of D transitions at early probe delays, i.e. until the photoactivated retinal is only partially rotated along the central double bond. In fact, at twisting angles slightly larger than 30° the $S_1 \rightarrow S_2$ PA signals are expected to blue-shift with respect to the FC region and to overlap with the red-shifting SE signal, disappearing from the NIR probe spectral window. At twisting angles around 60°, the $S_1 \rightarrow S_2$ transition is falling in the visible red region and should be detectable with the 2DVis(blue/red) setup (Fig. 14(a)). The time-resolved 2DVis(blue/red) spectra, indeed, are predicted to resolve $S_1 \rightarrow S_3$ and $S_1 \rightarrow S_4$ PAs, i.e. peaks 3 and 4, in the FC region. Upon bond relaxation, the peak 4 blue-shifts to the green and the $S_1 \rightarrow S_3$ PA signal is cancelled by the overlapping red-shifting SE. Peak 3 is expected to recover at 30° and to slowly blue-shift at larger twisting angles (peak 3'). Instead, the D' signals associated with the important $S_1 \rightarrow S_2$ transition (at twisting angles larger than 30°) is expected to quickly undergo very large blue-shift (from the near-IR to the UV while the chromophore rotates from 30° to 90°). Thus, the $S_1 \rightarrow S_2$ transition can be observed only transiently with a 2DVis(blue/red) setup whereas the 2DVis/NIR should ensure stable $S_1 \rightarrow S_2$ signals during the early stage of the photoisomerization reaction.

If one assumes that the photochemistry of retinal chromophores in solution follows a three-state mechanism, the S_1/S_2 energy gap is expected to be very small and consequently the $S_1 \rightarrow S_2$ PAs will not be detectable in time-resolved 2DES (one- or two-colours) experiments. Therefore, the comparison between the 2D *two-colour* spectra of Rh and those of retinal chromophores in solution could already provide evidences of environment-dependent photoisomerization mechanism of retinals. However, in order to directly detect the $S_1 \rightarrow S_2$ transitions during a *three-state* photoisomerization reaction, more elaborate multi-pulse techniques would be required. We have recently proposed[99] transient 2DES for direct detection of $S_0 \rightarrow S_2$ transitions along the retinal photoisomerization pathway. This subclass of fifth-order non-linear experiments involves a femtosecond actinic UV/Vis pulse to trigger the photochemical reaction and 2DES spectroscopy to obtain the 2DES of the generated transient molecular state. Such sequence of laser pulses allows for concomitant detection of $S_0 \rightarrow S_1$ and $S_0 \rightarrow S_2$ transitions along the S_1 photoisomerization path, by exploiting the transient population of the ground state during the photoreaction. Thereby, the time dependent S_1/S_2 energy gap can be resolved spectroscopically by monitoring the crossing/splitting of the $S_0 \rightarrow S_1$ and $S_0 \rightarrow S_2$ PA signals, shedding light on the role of covalent/ionic states interplay in retinal photochemistry.

It is important to note that the simulated time-resolved 2DES spectra reported in this work still represent a coarse picture of the experimental spectra since, here, we assume that during time intervals t_1 and t_3 the electronic energy levels remain fixed, i.e. we record "static" snapshots of the photoisomerizing chromophore. To follow more precisely the evolution of the excited states manifold during a real measurement, a more complex non-adiabatic propagation of the eigenstates should be performed, which will be the object of future work. Here, we also suggest transient 2DES spectroscopy as the ultimate experiment to track the relative positions of the ionic and covalent excited states (S_1 and S_2) along the photoisomerization path of retinals in different environments.

Conclusions

In this paper we have provided an overview of recent experimental and computational results aimed at exposing the primary photochemical reaction driving the visual process in higher animals: the *cis-trans* isomerization of the retinal chromophore in Rh. Thanks to advances in ultrafast optical spectroscopy, with the generation of broadly tunable few-optical-cycle light pulses[46] and the introduction of the FSRS technique[53], it is now possible to track the photoisomerization process of Rh with an unprecedented level of detail. Such progress in experimental techniques has been matched by advances in computational methods, with the introduction of QM/MM methods that allow *ab initio* simulations with accuracy sufficient to allow comparison with experimental data. We have now gained a much deeper understanding of the process, having achieved direct observation of the wavepacket motion through the CI[81] and the subsequent structural evolution on the photoproduct ground state[84]. Despite these successes, there is still ample room for additional work on visual rhodopsins, thanks to the development of novel sophisticated experimental techniques and computational methods. 2DES is now established in many research laboratories and it will be interesting to see experimental verification of the computational results presented in the previous paragraph. The continuous development of ultrafast structural dynamics techniques, such as femtosecond X-ray (also related to free electron lasers) and electron diffraction, will one day enable to achieve the chemist's dream of shooting a real-time movie of the isomerization process. Finally, a very interesting experimental challenge will be achieving coherent control[100] of the Rh

isomerization process, in order to verify whether it is possible to exceed the already remarkable efficiency of the natural reaction.

Acknowledgements

GC and MG acknowledge support by the European Research Council Advanced Grant STRATUS (ERC-2011-AdG No. 291198). MG and IR gratefully acknowledge support from the PSMN (Pôle Scientifique de Modélisation Numérique) computing center of ENS de Lyon.

Notes and references

[a] IFN-CNR, Dipartimento di Fisica, Politecnico di Milano, Piazza L. da Vinci 32, 20133 Milano, Italy.
[b] Université de Lyon, CNRS, Institut de Chimie de Lyon, École Normale Supérieure de Lyon, 46 Allée d'Italie, F-69364 Lyon Cedex 07, France.
[c] Dipartimento di Chimica "G. Ciamician", Università di Bologna, V. F. Selmi 2, 40126 Bologna, Italy.
[d] Institut für Theoretische Chemie und Computerchemie, Heinrich-Heine-Universität Düsseldorf, Universitätsstr. 1, 40225 Düsseldorf, Germany.

1 O.P. Ernst, D.T. Lodowski, M. Elstner, P. Hegemann, L.S. Brown, H. Kandori, *Chem. Rev.*, 2014, **114**, 126.
2 J.L. Spudich, C.S. Yang, K.H. Jung, E.N. Spudich, *Annu. Rev. Cell Dev. Biol.*, 2000, **16**, 365.
3 D. Oesterhelt and W. Stoeckenius, *Nature New Biology*, 1971, **233**, 149.
4 W. Stoeckenius, *Trends Biochem. Sci.*, 1985, **10**, 483.
5 O.A. Sineshchekov, K.-H. Jung, J.L. Spudich, *Proc. Natl. Acad. Sci. U. S. A.*, 2002, **99**, 8989.
6 F. Zhang, J. Vierock, O. Yizhar, L.E. Fenno, S. Tsunoda, A. Kianianmomeni, M. Prigge, A. Berndt, J. Cushman, J. Polle, J. Magnuson, P. Hegemann, and K. Deisseroth, *Cell*, 2011, **147**, 1446.
7 A. Terakita, *Genome Biol.*, 2005, **6**, 213.
8 M.B. Nielsen, *Chem. Soc. Rev.*, 2009, **38**, 913.
9 D. Baylor, *Proc. Natl. Acad. Sci. U. S. A.*, 1996, **93**, 560.
10 A. Wand, I. Gdor,1 J. Zhu, M. Sheves, and S. Ruhman, *Annu. Rev. Phys. Chem.*, 2013, **64**, 437.
11 T. Yoshizawa and G. Wald, *Nature*, 1963, **197**, 1279.
12 R.W. Schoenlein, L. A. Peteanu, R. A. Mathies and C. V. Shank, *Science*, 1991, **254**, 412.
13 R. A. Mathies, C. H. B. Cruz, W. T. Pollard and C. V. Shank, *Science*, 1988, **240**, 777.
14 R. Govindjee, S.P. Balshov, and T.G. Ebrey, *Biophys. J.*, 1990, **58**, 597.
15 J.E. Kim, M.J. Tauber, and R.A. Mathies, *Biochemistry*, 2001, **40**, 13774.
16 H. Kandori, Y. Katsuta, M. Ito and H. Sasabe, *J. Am. Chem. Soc*., 1995, **117**, 2669.
17 S. L. Logunov, L. Song and M. A. ElSayed, *J. Phys. Chem.*, 1996, **100**, 18586.
18 P. Hamm, M. Zurek, T. Roschinger, H. Patzelt, D. Oesterhelt and W. Zinth, *Chem. Phys. Lett.*, 1996, **263**, 613.
19 R. S. Becker and K. Freedman, *J. Am. Chem. Soc.*, 1985, **107**, 1477.
20 R. R. Birge, *Annu. Rev. Phys. Chem.*, 1990, **41**, 683.
21 F. Lumento, V. Zanirato, S. Fusi, E. Busi, L. Latterini, F. Elisei, A. Sinicropi, T. Andruniow, N. Ferre, R. Basosi and M. Olivucci, *Angew. Chem., Int. Ed.*, 2007, **46**, 414.
22 A. Sinicropi, E. Martin, M. Ryazantsev, J. Helbing, J. Briand, D. Sharma, J. Léonard, S. Haacke, A. Cannizzo, M. Chergui, V. Zanirato, S. Fusi, F. Santoro, R. Basosi, N. Ferré, and M. Olivucci, *Proc. Natl. Acad. Sci. U. S. A.*, 2008, **105**, 17642.
23 D.J. Tannor, *Introduction to Quantum Mechanics: A Time Dependent Perspective*, University Science Press, Sausalito, 2007.
24 M. Garavelli, P. Celani, F. Bernardi, M.A. Robb, and M. Olivucci, *J. Am. Chem. Soc.*, 1997, **119**, 6891.
25 R. Gonzalez-Luque, M. Garavelli, F. Bernardi, M. Merchan, M.A. Robb, and M. Olivucci, *Proc. Natl. Acad. Sci. USA* , 2000, **97,** 9379.
26 M. Klessinger and J. Michl, *Excited States and Photochemistry of Organic Molecules*, VCH Publishers, New York, 1994.
27 B.G. Levine and T.M. Martinez, *Annu. Rev. Phys. Chem.*, 2007, **58**, 613.
28 T.J. Martinez, *Nature*, 2010, **467**, 412.
29 F. Gai, K. C. Hasson, and P. A. Anfinrud, *Proc. Natl. Acad. Sci. USA*, 1996, **93**, 15124.
30 F. Gai, K. C. Hasson, J. C. McDonald and P. A. Anfinrud, *Science*, 1998, **279**, 1886.
31 T. Kobayashi, T. Saito, and H. Otani, *Nature*, 2001, **414**, 531.
32 S. Ruhman, B.X. Hou, N. Friedman, M. Ottolenghi, and M. Sheves, *J. Am. Chem. Soc.*, 2002, **124**, 8854.
33 M. Olivucci, A. Lami, and F. Santoro, *Angew. Chem. Int. Ed.*, 2005, **44**, 5118.
34 A. Kahan, O. Nahmias, N. Friedman, M. Sheves, and S. Ruhman, *J. Am. Chem. Soc.*, 2007, **129**, 537.
35 B. Loevsky, A. Wand, O. Bismuth, N. Friedman, M. Sheves, and S Ruhman, *J. Am. Chem. Soc.*, 2011, **133**, 1626.
36 J. B. Hurley, T. G. Ebrey, B. Honig and M. Ottolenghi, *Nature*, 1977, **270**, 540.
37 R.R. Birge, *Biochim. Biophys. Acta*, 1990, **1016**, 293.
38 L. Song and M. El-Sayed, *J. Am. Chem. Soc.*, 1998, **120**, 8889.
39 J. Herbst, K. Heyne and R. Diller, Science, 2002, 297, 822.
40 A. Warshel and Z.T. Chu, *J. Phys. Chem. B*, 2001, **105**, 9587.
41 A. Cembran, F. Bernardi, M. Olivucci, and M. Garavelli, *Proc. Natl. Acad. Sci. USA*, 2005, **102**, 6255.
42 S. A. Kovalenko, A. L. Dobryakov, J. Ruthmann, and N. P. Ernsting, *Phys. Rev. A*, 1999, **59**, 2369.
43 Z. Vardeny, J. Tauc, *Opt. Commun.*, 1981, **39**, 396.
44 D. Polli, D. Brida, S. Mukamel, G. Lanzani, and G. Cerullo, *Phys. Rev. A*, 2010, **82**, 053809.
45 G. Cerullo and S. De Silvestri, *Rev. Sci. Instrum.*, 2003, **74**, 1.
46 D. Brida, C. Manzoni, G. Cirmi, M. Marangoni, S. Bonora , P. Villoresi, S. De Silvestri, and G Cerullo, *J. Opt.*, 2010, **12**, 013001.
47 C. Manzoni, D. Polli, and G. Cerullo, *Rev. Sci. Instrum.* 2006, **77**, 023103.
48 D. Polli, L. Lüer, and G. Cerullo, *Rev. Sci. Instrum.* 2007, **78**, 103108.

49 M. Bargheer, N. Zhavoronkov, M. Woerner, T. Elsaesser, *ChemPhysChem*, 2006, **7**, pp. 783.
50 M. Gao, C. Lu, H. Jean-Ruel, L.C. Liu, A. Marx, K. Onda, S. Koshihara, Y. Nakano, X. Shao, T. Hiramatsu, G. Saito, H. Yamochi, R.R. Cooney, G. Moriena, G. Sciaini, and R.J. Dwayne Miller, *Nature*, 2013, **496**, 343.
51 D.W. McCamant, P. Kukura, and R.A. Mathies, *J. Phys. Chem. A*, 2003, **107**, 8208.
52 D.W. McCamant, P. Kukura, S. Yoon, and R.A. Mathies, *Rev. Sci. Instrum.*, 2004. **75**, 4971.
53 P. Kukura, D.W. McCamant, and R.A. Mathies, *Annu. Rev. Phys. Chem.*, 2007. **58**, 461.
54 C. Fang, R.R. Frontiera, R. Tran, and R.A. Mathies, *Nature*, 2009, **462**, 200.
55 T. Brixner, J. Stenger, H.M. Vaswani, M. Cho, R.E. Blankenship, and G.R. Fleming, *Nature*, 2005, **434**, 625.
56 E. Collini, C. Y. Wong, K. E. Wilk, P. M. G. Curmi, P. Brumer, and G. D. Scholes, *Nature*, 2010, **463**, 644.
57 S. Mukamel, *Annu. Rev. Phys. Chem.*, 2000, **51**, 691.
58 P. Hamm, M. Zanni, *Concepts and Methods of 2D Infrared Spectroscopy*, Cambridge University Press, 2011.
59 M.L. Cowan, J.P. Ogilvie, and R.J.D. Miller, *Chem. Phys. Lett.*, 2004, **386**, 184.
60 T. Brixner, I. V. Stiopkin, and G. R. Fleming, *Opt. Lett.*, 2004, **29**, 884.
61 S. H. Shim, D. B. Strasfeld, Y. L. Ling, and M. T. Zanni, *Proc. Natl. Acad. Sci. USA*, 2007, **104**, 14197.
62 E. M. Grumstrup, S. H. Shim, M. A. Montgomery, N. H. Damrauer, and M. T. Zanni, *Opt. Express*, 2007, **15**, 16681.
63 P. F. Tekavec, J. A. Myers, K. L. M. Lewis, and J. P. Ogilvie, *Opt. Lett.*, 2009, **34**, 1390.
64 D. Brida, C. Manzoni, and G. Cerullo, *Opt. Lett.*, 2012, **37**, 3027.
65 M. Olivucci (ed.), *Computational Photochemistry*, Elsevier, Amsterdam, Vol. 16, 2005.
66 K. Andersson, P.-A. Malmqvist, B. O. Roos, *J. Chem. Phys.*, 1992, **96**, 1218.
67 I. Rivalta, A. Nenov, G. Cerullo, S. Mukamel and M. Garavelli, *Int. J. Quantum Chem.*, 2014, **114**, 85.
68 A. Nenov, I. Rivalta, G. Cerullo, S. Mukamel and M. Garavelli, *J. Phys. Chem. Lett.*, 2014, **5**, 767.
69 P. Altoè, M. Stenta, A. Bottoni, and M. Garavelli, *Theor. Chem. Acc.*, 2007, **118**, 219.
70 G. Groenhof et al., *Adv. Quantum Chem.*, 2010, **59**, 181.
71 H.M. Senn and W. Thiel, *Top. Curr. Chem.*, 2007, **268**, 173.
72 P. Cieplak, F.-Y. Dupradeau, Y. Duan, and J. Wang, *Phys. Cond. Mat.*, 2009, **21**, 333102.
73 W. Chen, L. Hase, and B. Schlegel, *Chem. Phys. Lett.*, 1994, **228**, 436.
74 B.H. Lengsfield and D.R. Yarkony, *Adv. Chem. Phys.*, 1992, **82**, 1.
75 J. Stalring, B. Anders, and R. Lindh, *Mol. Phys.*, 2001, **99**, 103.
76 L. Verlet, *Phys. Rev.*, 1967, **159**, 98.
77 J. C. Tully, *Int. J. Quant. Chem.*, 1991, **40**, 299.
78 E. Fabiano, T.W. Keal, and W. Thiel, *Chem. Phys.*, 2008, **349**, 334.
79 G. Granucci and M. Persico, *J. Chem. Phys.*, 2007, **126**, 134114.
80 W.J. DeGrip, F.J.M. Daemen, and S.L. Bonting, *Methods in Enzymology*, 1980, **67**, 301.
81 D. Polli, P. Altoe, O. Weingart, K.M. Spillane, C. Manzoni, D. Brida, G. Tomasello, G. Orlandi, P. Kukura, R.A. Mathies, M. Garavelli and G. Cerullo, *Nature*, 2010, **467**, 440.
82 L.A. Peteanu, R.W. Schoenlein, Q. Wang, R.A. Mathies, C.V. Shank, *Proc. Natl. Acad. Sci. USA*, 1993, **90**, 11762.
83 Q. Wang, R. W. Schoenlein, L. A. Peteanu, R. A. Mathies and C. V. Shank, *Science*, 1994, **266**, 422.
84 P. Kukura, D.W. McCamant, S. Yoon, D.B. Wandschneider, and R.A. Mathies, *Science*, 2005, **310**, 1006.
85 A. Warshel, *Nature*, 1976, **260**, 679.
86 A. Warshel and N. Barboy, *J. Am. Chem. Soc.*, 1982, **104**, 1469.
87 T. Okada, M. Sugihara, A.N. Bondar, M. Elstner, P. Entel, and V. Buss, *J. Mol. Biol.*, 2004, **342**, 571.
88 R.W. Schoenlein, L.A. Peteanu, Q. Wang, R.A. Mathies, C.V. Shank, *J. Phys. Chem.*, 1993, **97**, 12087.
89 J. Fan, B. Rohrer, G. Moiseyev, J. Ma, R.K. Crouch, *Proc. Natl. Acad. Sci. U.S.A.*, 2003, **100**, 13662.
90 T. Yoshizawa and G. Wald, *Nature*, 1963, **197**, 1279.
91 S.J. Hug, J.W. Lewis, and D.S. Kliger, *J. Am. Chem. Soc.*, 1988, **110**, 1998.
92 D. Polli, O. Weingart, D. Brida, E. Poli, M. Maiuri, K. M. Spillane, A. Bottoni, P. Kukura, R. A. Mathies, G. Cerullo and M. Garavelli, *Angew. Chem. Int. Ed.*, 2014, **53**, 2504.
93 W. C. Chung, S. Nanbu, T. Ishida, *J. Phys. Chem. B*, 2012, **116**, 8009.
94 A. Strambi, P. B. Coto, L. M. Frutos, N. Ferré, M. Olivucci, *J. Am. Chem. Soc.*, 2008, **130**, 3382.
95 J.D. Biggs and S. Mukamel, *J. Chem. Phys.*, 2011, **134**, 161101.
96 E.C.Y. Yan, Z. Ganim, M.A. Kazmi, B.S.W. Chang, T.P. Sakmar, and R.A. Mathies, *Biochemistry*, 2004, **43**, 10867.
97 I. Rivalta, A. Nenov, O. Weingart, G. Cerullo, M. Garavelli, and S Mukamel, *J. Phys. Chem. B*, 2014, **118**, 8396.
98 G. Zgrablic, K. Voitchovsky, M. Kindermann, S. Haacke, and M. Chergui, *Biophys. J.*, 2005, **88**, 2779.
99 I. Rivalta, A. Nenov, and M. Garavelli, *Phys. Chem. Chem. Phys.*, 2014, **16**, 16865.
100 V.I. Prokhorenko, A.M. Nagy, S.A. Waschuk, L.S. Brown, R.R. Birge, and R.J.D. Miller, *Science*, 2006, **313**, 1257.

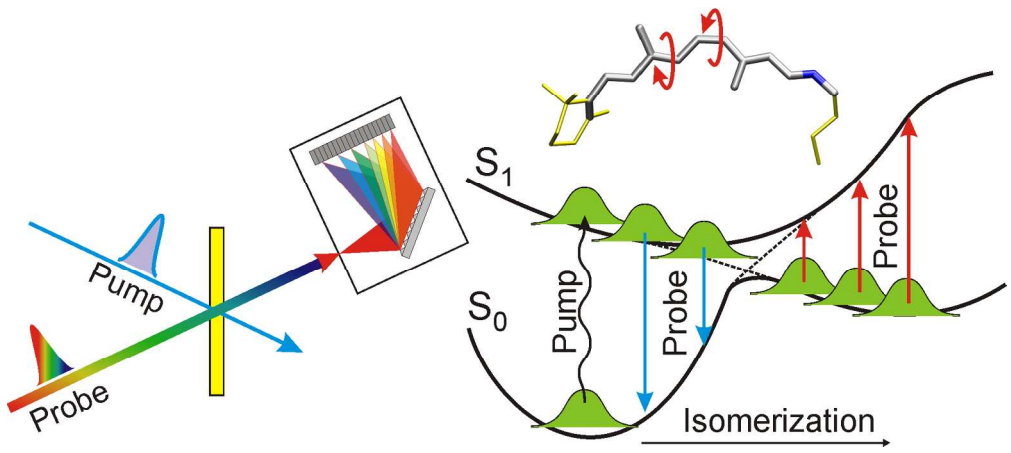

Graphical abstract
169x74mm (300 x 300 DPI)